Yi Yang, Ching Tai Ng, Munawwar Mohabuth and Andrei Kotousov

Finite element prediction of acoustoelastic effect associated with Lamb wave propagation in pre-stressed plates

Smart Materials and Structures, 2019; 28(9):095007-1-095007-11

Finite Element Prediction of Acoustoelastic Effect Associated with Lamb Wave Propagation in Pre-stressed Plates

Yi Yang[1], Ching Tai Ng[1,*], Munawwar Mohabuth[2], Andrei Kotousov[2]

[1] School of Civil, Environmental & Mining Engineering, The University of Adelaide, SA 5005, Australia

[2] School of Mechanical Engineering, The University of Adelaide, SA 5005, Australia

Abstract

The paper presents outcomes of a finite element (FE) study of acoustoelastic effect associated with Lamb wave propagation in plates subjected to homogeneous bi-axial and bending stresses. In particular, the change of the phase velocity of the fundamental Lamb wave modes is obtained for different stress levels, bi-axial stress ratios and wave propagation angles. A comparison of the obtained numerical results with an analytical solution demonstrates a very good agreement. Moreover, the influence of bending stress on the wave velocities and wave front profile is further investigated numerically. There are currently no analytical results for this case. The developed and verified FE modelling approach can help to address several issues in the current non-destructive inspections including: in the investigation of changing stress conditions on the defect detection as well as in an adaptation of the existing Lamb wave-based defect evaluation systems to monitoring of stress too. The latter may have many benefits from sharing the same hardware for the purpose of maintaining structural integrity of thin-walled structural components.

[*] Email: alex.ng@adelaide.edu.au

Keywords: Acoustoelasticity, Lamb waves, pre-stressed plate, finite element, structural health monitoring

1. Introduction

1.1. Structural Health Monitoring using guided waves

Structural health monitoring (SHM) has attracted significant attention in the last two decades. Different damage detection methods were developed and widely documented the literature [1]-[4]. In particular, the use of ultrasonic guided waves has proved to be one of the promising methods for detecting damage [5]-[8], specifically, with respect to the fundamental modes of Lamb [9][10] and non-dispersive Rayleigh waves [11]-[13]. Other studies were largely focused on understanding of guided wave interactions with and scattering at various types of defects [14]-[16]. Practical implementation of these theoretical results for damage detection can be found in [17]-[20].

The focus of the current study are Lamb waves, which is a special type of ultrasonic guided waves, which can propagate in thin-walled structures with stress-free lateral surfaces. The main feature of Lamb waves is their ability to travel over long distances with a very little energy loss. Many previous studies reported an excellent sensitivity of these waves to the presence of damage in different metallic and composite structures such as beams [21],[22], plates [23],[24], pipes [25],[26] as well in structures made of concrete [27]. These studies also demonstrated that Lamb waves have a great potential for development of cost-effective methods for non-destructive safety inspections or on-line monitoring systems [28],[29].

Over the last decade, a wide range of damage detection methods was developed using Lamb waves. A large class of these methods rely on a comparison of the actual signal response with a reference signal obtained for defect-free conditions, e.g. in the beginning of the operation or after a factory defect control. It was demonstrated that a simple subtraction of the actual and reference signals, i.e. the residual signal, can provide the required information needed for the damage detection and its evaluation [30],[31]. However, changing environmental and operational conditions [32],[33], such as temperature and stress, can mask the signal alterations caused by the damage [34]. The effects of changing environmental and operational conditions on damage detection is currently considered as one of the main reasons why the damage detection techniques developed in the laboratory environment are not readily transferable to the real-world applications. In the literature, a number of techniques were developed to compensate the error due to unavoidable variations in temperature and loading conditions during operation and inspections [35],[36]. Alternatively, some researchers have suggested the nonlinear methods for the damage detection, which do not need a reference signal [37]-[39]. However, it is very difficult to evaluate the severity of the damage with such non-linear methods.

One solution to the environmental changes can be the development of a procedure for the compensation of environmental and operational conditions based on a computational model, e.g. FE modelling. Subsequently, the focus of the current paper is the investigation of the effect of the applied stress on the propagation of Lamb waves as the effect of the temperature was investigated elsewhere. This effect is commonly known as the acoustoelastic effect. The next subsection will provide a brief state of the art review of the acoustoelastic effect associated with the Lamb wave propagation in pre-stressed plates.

1.2. Acoustoelastic effect of Lamb wave propagation

Acoustoelastic effect is defined as the effect of the applied stress on the wave propagation in a media. It has been studied since the development of the finite deformation theory by Murnaghan [40], who formulated the material nonlinearity using third order elastic constants. Some pioneering studies in this area include the research of Hughes and Kelly [41], who derived equations relating the wave velocity to the applied stress and experimentally measured the acoustoelastic effect. Another experimental study of Egle and Bray [42] demonstrated how to obtain higher-order elastic constants from experiments with bulk waves.

In the literature, many developments and studies in the acoustoelasticity mainly focused on and utilised bulk waves (Pau and Scalea [43]). The acoustoelastic effect is usually quantified by measuring the velocity change of the propagating wave in pre-stressed media. However, the velocity change of ultrasonic bulk wave due to the applied stress is small (Mohabuth *et al*. [44]). In recent years, guided waves have attracted increasing practical interests due to its high sensitivity to stress, changes of material properties and its ability to propagate over long distances. Gandhi *et al.* [45] provided a comprehensive analysis of the acoustoelastic effect due to bi-axial loading through analytical formulation and experimental measurements. However, their work only considered the first order of the infinitesimal strain tensor. In a more recent study by Mohabuth *et al*. [44], they developed the governing equation for the propagation of small amplitude waves in a pre-stressed plate using the theory of incremental deformations superimposed on large deformation. The development was extended to estimate the effect of applied or thermally-induced stresses on the Lamb wave propagation [46]. In similar time, Packo *et al*. [47] studied the dispersion of the finite amplitude Lamb wave in nonlinear plates with the consideration of up to fourth-order elastic constants.

An analysis of geometrically complicated structures or structures subjected to complex loadings is very difficult or not possible using analytical approaches. All theoretical results were obtained for infinite plates subjected to simple homogeneous stress states. Therefore, in this context, it is important to develop a numerical method in order to analyse more complex and more relevant practical situations.

In the current study, a VUMAT subroutine is developed in ABAQUS based on Murnaghan's energy function [40] to model the Lamb wave propagation in pre-stressed plates. The FE model is verified by comparing the numerical results for the phase velocities with the analytical results obtained by Mohabuth *et al*. [44]. The verified FE model is then utilised to predict the acoustoelastic effect of Lamb wave propagation in plates subjected to bending.

The current paper is structured as follows. In Section 2, a theoretical basis of the acoustoelastic effect of Lamb wave is elaborated, followed by a derivation of the constitutive equation to develop the material nonlinearity in ABAQUS VUMAT in Section 3. Then, the FE model with nonlinear material is developed in Section 4, and the simulation results of the FE model is verified by comparing them with the theoretical solutions obtained from previous studies. A series of case studies is then carried out using the verified FE model in Section 5, which considers the acoustoelastic effect of Lamb wave on a plate under bending. Finally, conclusions from the numerical studies are drawn in Section 6.

2. Governing equations for acoustoelastic Lamb wave propagation

According to Mohabuth *et al*. [44], the position of the material particle in the reference (β_r) and current (β_0) configurations is denoted by $\boldsymbol{X}$ and $\boldsymbol{x}$, respectively. The deformation gradient **F** is defined by

$$\mathbf{F} = \frac{\partial \mathbf{x}}{\partial \mathbf{X}} \tag{1}$$

The nominal and Cauchy stress tensors are given by

$$\mathbf{S} = \frac{\partial W}{\partial \mathrm{F}}, \boldsymbol{\sigma} = J^{-1}\mathrm{F}\frac{\partial W}{\partial \mathrm{F}} \tag{2}$$

where W is the strain energy function and $J = \det\mathbf{F}$. In the study of Mohabuth *et al*. [44], the strain energy function is defined by deformation gradient. The corresponding incremental constitutive equation of the stress tensor is given in component form by

$$\hat{\mathrm{S}}_{0_{\mathrm{pi}}} = \mathrm{A}_{0_{\mathrm{piqj}}} u_{\mathrm{j,q}} \tag{3}$$

where $\hat{\mathrm{S}}_{0_{\mathrm{pi}}}$ are the components of the incremental nominal stress tensor. $\mathrm{A}_{0_{\mathrm{piqj}}}$ are the components of the fourth-order elasticity tensor of instantaneous elastic moduli [44], [45]. u is the displacement vector relative to β_0, and a comma indicates partial differentiation with respect to Eulerian coordinate.

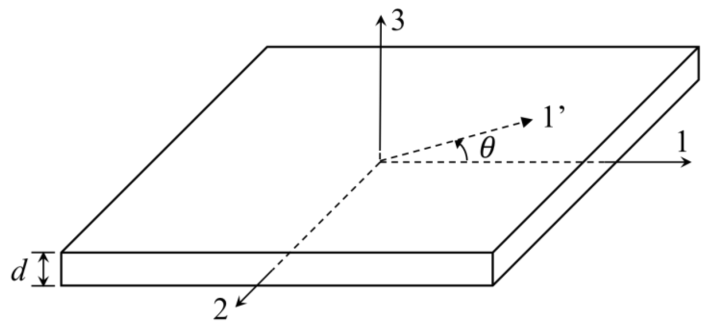

Figure 1: Cartesian coordinate system defined in the mid-plane of the plate with stresses applied in axes 1 and 2 direction and Lamb wave propagation in axis 1' direction

As shown in Figure 1, consider an isotropic plate with density of ρ defined in a Cartesian coordinate system located at the mid-plane of the plate. The equation of motion in a prestressed plate is given by

$$A_{0piqj}\,\frac{\partial^2 u_j}{\partial x_p \partial x_q} = \rho\frac{\partial^2 u_i}{\partial t^2} \tag{4}$$

When considering a Lamb wave propagating along a axis 1' direction with an angle of θ, the equation of motion can be transformed to the rotated coordinate system

$$A_{0piqj}^{'}\,\frac{\partial^2 u_j^{'}}{\partial x_p^{'} \partial x_q^{'}} = \rho\frac{\partial^2 u_i^{'}}{\partial t^2} \tag{5}$$

and the relationship between the two elasticity tensors before and after transformation is

$$A_{0piqj}^{'} = \beta_{pr}\beta_{ik}\beta_{qs}\beta_{jl}A_{0rksl} \tag{6}$$

where β_{ij} is the cosine of the angle of rotation. In the following discussions, all the equations are formulated based on the original coordinate system.

The wave motion is assumed as

$$u_j = U_j e^{i\xi(\boldsymbol{x_1+\alpha x_3-ct})} \tag{7}$$

where ξ is the wave number in x_1 direction, c is the phase velocity along x_1 direction, and α is the ratio of x_3 wavenumber to x_1 wavenumber. Substitute the equation to the equation of motion yields the Christoffel equations

$$\mathrm{K_{ij}U_j} = 0 \tag{8}$$

and the parameters $\mathrm{K_{ij}}$ are given by

$$\begin{aligned}
\mathrm{K_{11}} &= \rho c^2 - \mathrm{A_{01111}} - \alpha^2 A_{01313},\\
\mathrm{K_{22}} &= \rho c^2 - \mathrm{A_{01212}} - \alpha^2 A_{02323},\\
\mathrm{K_{33}} &= \rho c^2 - \mathrm{A_{01313}} - \alpha^2 A_{03333},\\
\mathrm{K_{12}} = \mathrm{K_{21}} &= -\mathrm{A_{01112}} - \alpha^2 A_{01323},\\
\mathrm{K_{13}} = \mathrm{K_{31}} &= -\alpha(A_{01133} + A_{01331}),\\
\mathrm{K_{23}} = \mathrm{K_{32}} &= -\alpha(A_{01233} + A_{01332}),
\end{aligned} \tag{9}$$

For non-trivial solutions of the displacement amplitude $\mathrm{U_j}$, the determinant of the K matrix goes to zero. This yields a sixth order equation with six solutions α_q, $q \in \{1,2,3,4,5,6\}$, which is expressed as

$$\mathrm{P_6}\alpha^6 + \mathrm{P_4}\alpha^4 + \mathrm{P_2}\alpha^2 + \mathrm{P_0} = 0 \tag{10}$$

where the coefficients can be found in [48]. To satisfy the stress-free boundary condition, the approach developed in the work of Nayfeh and Chimenti [48], and the displacement ratios between $\mathrm{U_2}$ to $\mathrm{U_1}$ and $\mathrm{U_3}$ to $\mathrm{U_1}$ are defined

$$\mathrm{V_q} = \frac{\mathrm{U_{2q}}}{\mathrm{U_{1q}}},\ \mathrm{W_q} = \frac{\mathrm{U_{3q}}}{\mathrm{U_{1q}}} \tag{11}$$

The expansion of V_q and W_q can also be found in the work of Nayfeh and Chimenti [48]. With the displacement ratios, the displacement filed of the Lamb waves can be written as

$$\begin{aligned}
\mathrm{u_1} &= \textstyle\sum_{q=1}^{6} \mathrm{U_{1q}} e^{i\xi(\mathbf{x_1}+\boldsymbol{\alpha_q}\mathbf{x_3}-\mathbf{ct})},\\
\mathrm{u_2} &= \textstyle\sum_{q=1}^{6} \mathrm{V}_q \mathrm{U_{1q}} e^{i\xi(\mathbf{x_1}+\boldsymbol{\alpha_q}\mathbf{x_3}-\mathbf{ct})},\\
\mathrm{u_3} &= \textstyle\sum_{q=1}^{6} W_q \mathrm{U_{1q}} e^{i\xi(\mathbf{x_1}+\boldsymbol{\alpha_q}\mathbf{x_3}-\mathbf{ct})},
\end{aligned} \tag{12}$$

Substitute the displacement relations to equation (3), gives the expression for stresses in 3 direction

$$\hat{S}_{33} = \sum_{q=1}^{6} i\xi D_{1q} U_{1q} e^{i\xi(x_1+\alpha_q x_3-ct)},$$

$$\hat{S}_{13} = \sum_{q=1}^{6} i\xi D_{2q} U_{1q} e^{i\xi(x_1+\alpha_q x_3-ct)},$$

$$\hat{S}_{23} = \sum_{q=1}^{6} i\xi D_{3q} U_{1q} e^{i\xi(x_1+\alpha_q x_3-ct)}, \tag{13}$$

where the coefficients D_{1q}, D_{2q} and D_{3q} are defined with the elasticity tensor and displacement ratios [48]. For the stress-free condition at the upper (*d*/2) and lower (-*d*/2) surfaces of the plate, there are six equations in terms of the amplitudes $U_{11}, U_{12}, \ldots, U_{16}$, and the determinant is

$$\begin{vmatrix} D_{11}E_1 & D_{12}E_2 & D_{13}E_3 & D_{14}E_4 & D_{15}E_5 & D_{16}E_6 \\ D_{21}E_1 & D_{22}E_2 & D_{23}E_3 & D_{24}E_4 & D_{25}E_5 & D_{26}E_6 \\ D_{31}E_1 & D_{32}E_2 & D_{33}E_3 & D_{34}E_4 & D_{35}E_5 & D_{36}E_6 \\ D_{11}\hat{E}_1 & D_{12}\hat{E}_2 & D_{13}\hat{E}_3 & D_{14}\hat{E}_4 & D_{15}\hat{E}_5 & D_{16}\hat{E}_6 \\ D_{21}\hat{E}_1 & D_{22}\hat{E}_2 & D_{23}\hat{E}_3 & D_{24}\hat{E}_4 & D_{25}\hat{E}_5 & D_{26}\hat{E}_6 \\ D_{31}\hat{E}_1 & D_{32}\hat{E}_2 & D_{33}\hat{E}_3 & D_{34}\hat{E}_4 & D_{35}\hat{E}_5 & D_{36}\hat{E}_6 \end{vmatrix} = 0 \tag{14}$$

where $\hat{E}_q = E_q^{-1} = e^{-i\xi\alpha_q \frac{d}{2}}$. The determinant leads to two uncoupled characteristic equation

$$D_{11}G_1 \cot(\gamma\alpha_1) - D_{13}G_3 \cot(\gamma\alpha_3) + D_{15}G_5 \cot(\gamma\alpha_5) = 0,$$

$$D_{11}G_1 \tan(\gamma\alpha_1) - D_{13}G_3 \tan(\gamma\alpha_3) + D_{15}G_5 \tan(\gamma\alpha_5) = 0, \tag{15}$$

corresponding to symmetric and anti-symmetric Lamb wave modes, respectively, and $\gamma = \xi\, d/2 = \omega d/2c$. The parameters G_i are provided in [48]. Consequently, with the elasticity tensor defined through nonlinear energy function and equation (15), the dispersion relation of Lamb wave can be obtained.

3. Implementation to ABAQUS/Explicit

In ABAQUS/Explicit, VUMAT can be used to define the mechanical constitutive behaviour based on the nonlinear strain energy function of Murnaghan [40], which is written as:

$$W(\mathbf{E}) = \frac{1}{2}(\lambda + 2\mu)i_1^2 - 2\mu i_2 + \frac{1}{3}(l+m)i_1^2 - 2m i_1 i_2 + n i_3 \tag{16}$$

where λ and μ are the lamé elastic constants; l, m and n are the third order elastic constants. $i_1 = tr\mathbf{E}$, $i_2 = \frac{1}{2}[i_1^2 - tr(\mathbf{E})^2]$, $i_3 = det\mathbf{E}$, respectively. **E** is the Green-Lagrange strain tensor given by:

$$\mathbf{E} = \frac{1}{2}(\mathbf{C} - \mathbf{I}) \tag{17}$$

where **I** is the identity tensor and **C** is the right Cauchy-Green deformation tensor, defined as:

$$\mathbf{C} = \mathbf{F}^{\mathrm{T}}\mathbf{F} = \mathbf{U}^{\mathbf{2}} \tag{18}$$

where **U** is the right stretch tensor.

In ABAQUS, the stress in VUMAT of ABAQUS/Explicit is the Cauchy stress tensor in Green-Naghdi basis,

$$\hat{\boldsymbol{\sigma}} = \mathbf{R}^{\mathrm{T}}\boldsymbol{\sigma}\mathbf{R} \tag{19}$$

where **R** is rotation tensor, and **R** is a proper orthogonal tensor, i.e., $\mathbf{R}^{-1} = \mathbf{R}^{\mathrm{T}}$. The relationship between **F**, **U** and **R** is given by

$$\mathbf{F} = \mathbf{R}\mathbf{U} \tag{20}$$

So, equation (19), with the energy function presented in equation (16) can be translated to,

$$\hat{\boldsymbol{\sigma}} = \mathrm{J}^{-1}\mathbf{R}^{\mathrm{T}}\mathbf{F}\mathbf{T}\mathbf{F}^{\mathrm{T}}\mathbf{R} = \mathrm{J}^{-1}\mathbf{R}^{\mathrm{T}}\mathbf{R}\mathbf{U}\mathbf{T}\mathbf{U}^{\mathrm{T}}\mathbf{R}^{\mathrm{T}}\mathbf{R} = \mathrm{J}^{-1}\mathbf{U}\frac{\partial W(\mathbf{E})}{\partial \mathbf{E}}\mathbf{U}^{\mathrm{T}} \tag{21}$$

where T is the second Piola-Kirchhoff (PK2) stress. The stress in VUMAT must be updated with the equation at the end (t+Δt) of an integration step and stored in stressNew(i), which is a default variable of the updated stress value at the end of each step. Based on the values of F and U given in the subroutine at the end of previous step (t), stressNew(i) can be obtained and then proceed to the next integration step.

4. Numerical Case Studies

4.1. 3D Finite Element Model

A 3D FE model of a 6061-T6 aluminium plate was developed with ABAQUS software and the wave propagation problem was solved by the explicit integration approach [50]. The material properties of the 6061-T6 aluminium are listed in Table 1. The thickness of the plate is 3.2mm and the in-plane dimension is 240mm×240mm. The element type used in the model is the 8-node linear brick with reduced integration, and hourglass control (C3D8R). The in-plane dimension of an element is 0.25×0.25mm^2 to ensure that there are at least 20 elements per wavelength [51]. There are 10 elements in the thickness direction, and hence, the thickness of each element is 0.32mm. To reduce the computational cost, only a quarter of the plate (120mm×120mm) is modelled using symmetric boundary conditions due to the symmetric nature of the FE model (Figure 2).

As shown in Figure 2, bi-axial stresses are applied to the plate, which are defined as σ_1 and σ_2, with

$$\sigma_2 = \lambda\sigma_1 \tag{22}$$

where λ is the bi-axial stress ratio. In this study, quasi-static loading with a duration of 2ms is used to apply the initial stress. The duration is sufficient to minimise the transient effect due to the loading process on the propagating wave modelling in the following steps. After the plate is stressed, the fundamental symmetric mode (S_0) of Lamb wave is excited by applying in-plane nodal displacements to nodes at the circumference of a quarter of 10mm diameter circle located at the bottom of the modelled quarter plate. The excitation signal is a 250kHz 4-cycle narrow-band sinusoidal tone burst pulse modulated by a Hann window. The measurements are taken in five different directions, i.e., 0°, 22.5°, 45°, 67.5° and 90°. There are six measurement points along each direction as specified in Figure 2. The first measurement point is 30mm away from the excitation area, and all the five other measurement points are equally spaced at 4mm.

Table 1: Material properties of 6061-T6 aluminium [49]

λ (GPa)	μ (GPa)	l (GPa)	m (GPa)	n (GPa)	Density (kg/m^3)
54.3	27.2	-281.5	-339.0	-416.0	2704

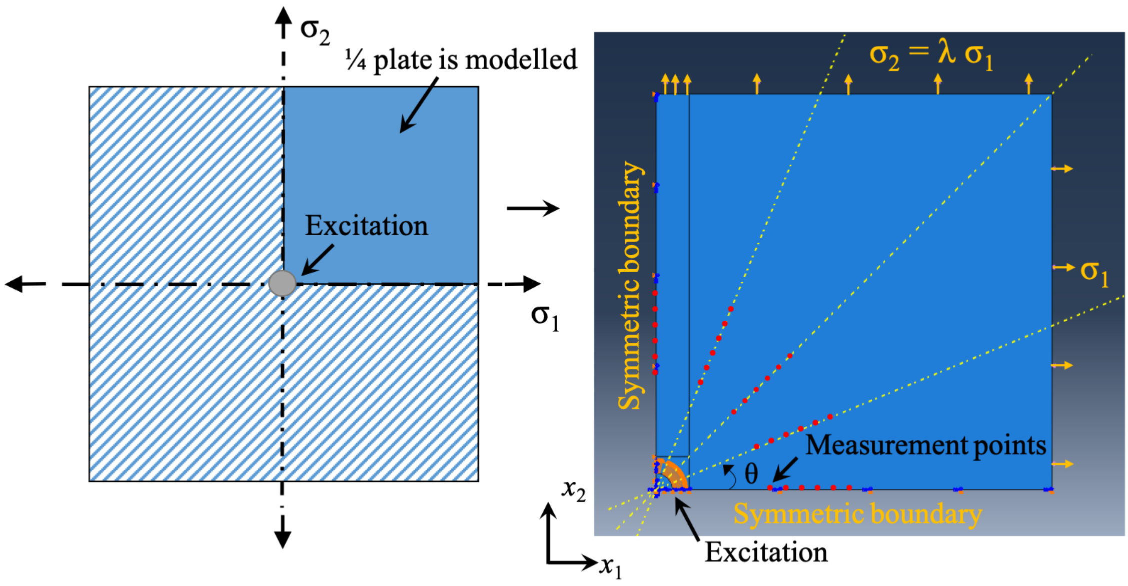

Figure 2: Schematic diagram of the FE model with applied stresses

4.2. Plate under bi-axial stress state

Figure 3 shows the time domain signal of the excited Lamb wave mode propagating in $\theta = 0°$ direction with linear material behaviour defined using standard elastic properties and nonlinear material behaviour defined in VUMAT, respectively. In the numerical results obtained from the nonlinear material model, there is a clear shift of the peak of the Lamb wave signal when the plate is subjected to an 80MPa bi-axial tension. In contrast, in the wave signals obtained from the linear material model, there is no shift of the peak no matter the model is subjected to stress or not.

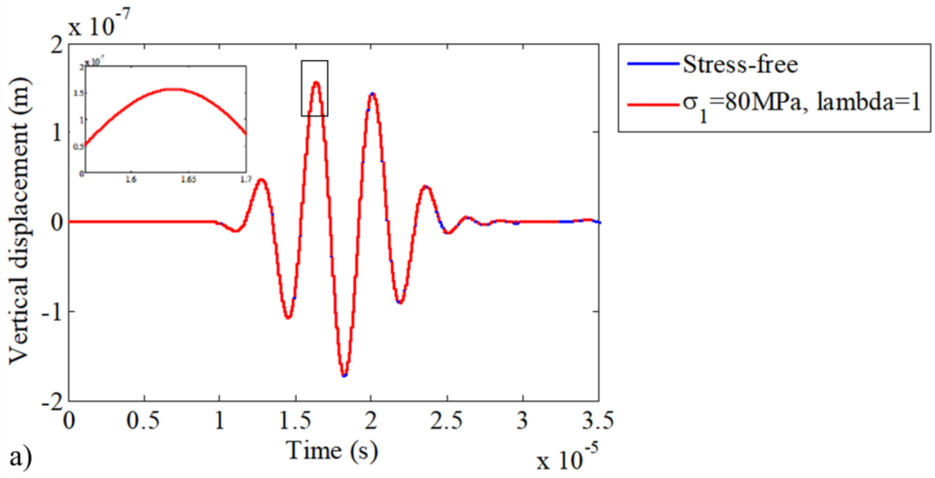

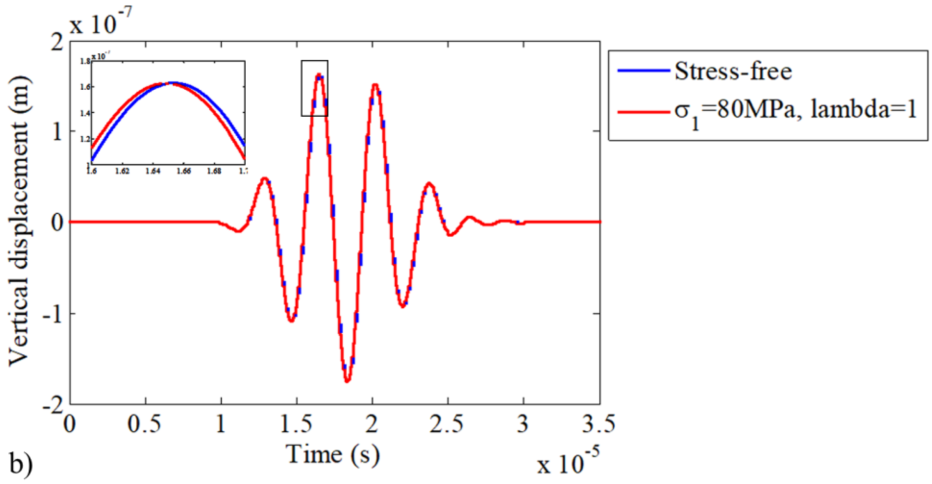

Figure 3: FE simulated Lamb wave signal at $\theta = 0°$ propagation direction in a plate with a) linear material properties and b) nonlinear material properties.

The propagating signals corresponding to S_0 Lamb wave mode are calculated in different wave propagation directions (θ), see Figure 2. By using these calculated data, the phase velocity can be evaluated by

$$C_p = \frac{2\pi f d}{\Delta\phi} \tag{23}$$

where C_p is the phase velocity, f is the excitation frequency, d is the distance between two adjacent measurement points, and $\Delta\phi$ is the phase change between the two measurement points. As the plate undergoes in-plane deformation due to pre-stress, the distance d used for the formula is the distance after the deformation. Five phase velocities are calculated in each direction, and the averaged value of the velocity is then calculated. The effect of the plate thickness change due to the Poisson's effect is not considered as the change of thickness is very small and its influence on phase velocity is negligible.

The dispersive nature of Lamb wave can introduce some additional errors to the velocity calculated from the FE model. According to the dispersion curve of the 6061-T61 aluminium plate of 3.2 mm thickness (Figure 4), the excitation frequency used in the simulation is selected in a region having relatively flat phase velocity profile so that the dispersive effect can be minimised. It can be seen in Figure 4 that the fundamental anti-symmetric mode (A_0) of Lamb wave at low frequency region (< 500kHz) and S_0 Lamb wave at frequency region of 500 – 1000kHz, as well as the higher order anti-symmetric and symmetric modes Lamb wave are very dispersive. In this study, the number of cycles of excitation signal is carefully selected so that the frequency bandwidth is reduced, while the reflected waves from boundary are not mixed with the first arrival. Thus the phase velocity change can be estimated accurately.

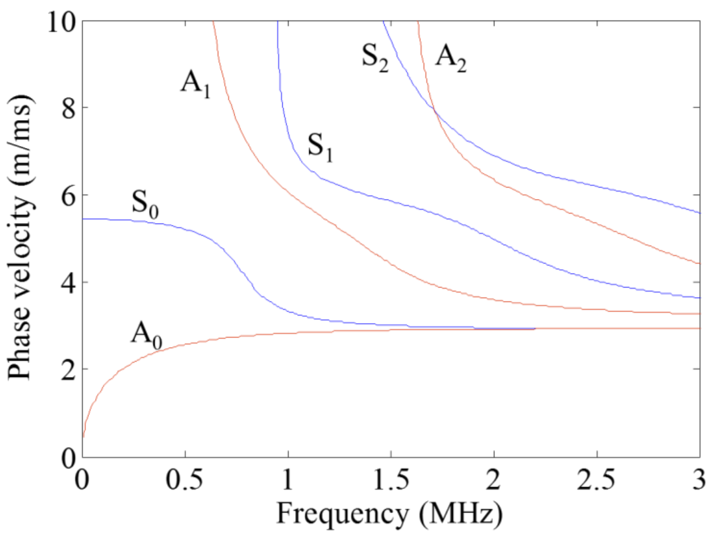

Figure 4: Phase velocity dispersion curve of 6061-T6 aluminium

Four cases are considered to verify the 3D FE model with the material nonlinearity. Case 1 investigates the effect of stress ratio λ, in which different values of λ are applied and σ_1 = 80MPa. Case 2 investigates the effect of stress magnitude, in which σ_1 = 80MPa and λ = -0.5 and -1. Case 3 studies the effect of the wave propagation angle, in which σ_1 = 0MPa, 20MPa, 40MPa, 60MPa and 80MPa and λ = -1, -0.5, 0, 0.5 and 1. Case 4 analyses the effect of the wave excitation frequency, in which the considered excitation frequency 200kHz (*fd* = 640kHz-mm) is different to the excitation frequencies considered in Cases 1 – 3 with different stress ratios λ and σ_1 =80MPa. Table 1 is a summary of these cases.

Table 1: Summary numerical case studies of biaxial stresses

	Investigation	σ_1 (MPa)	σ_2 (MPa)	λ	Excitation frequency
Case 1	Biaxial stress ratio λ effect	80	-80, -40, 0, 40, 80	-1,-0.5,0,0.5,1	250kHz
Case 2	Stress magnitude effect	0,20,40,60,80	0,-20,-40,-60,-80	-1	250kHz
		0,20,40,60,80	0,-10,-20,-30,-40	-0.5	250kHz
Case 3	Wave propagation angle effect	80	-80,-40,0,40,80	-1,-0.5,0,0.5,1	250kHz
Case 4	Wave excitation frequency effect	80	-80-40,0,-40,80	-1,-0.5,0,0.5,1	200kHz

In Case 1, the value of σ_2 is fixed at 80MPa while the values of σ_1 are -80MPa, -40MPa, 0MPa, 40MPa and 80MPa. The corresponding bi-axial stress ratios λ are -1, -0.5, 0, 0.5 and 1, respectively. Figure 5 shows the results of the phase velocity change against different values of bi-axial stress ratio λ. The analytical solutions calculated based on the equations developed in [44] and the 3D FE simulation results are shown in Figure 5, in which they are presented by solid and dash-dotted lines, respectively. There is very good agreement between the analytical solutions and FE simulation results for all wave propagation angles ($\theta = 0°, 22.5°, 45°, 67.5°$ and $90°$). The results also show that the phase velocity change has a linear relationship with the bi-axial stress ratios, which is predicted by the acoustoelastic theory. It should be noted that when the bi-axial stress ratio λ = 1, the phase velocity changes in all propagation directions are negative and having the same magnitude. In comparison, when λ =

-1, there is no velocity change in 45° direction, and for propagation directions in 22.5° and 67.5°, as well as 0° and 90°, the magnitude of velocity changes is the same but has opposite signs. It can be seen that, when λ is changed from -1 to 1, phase velocity change in 90° propagation direction experiences the largest variation, while in 22.5° direction the variation is trivial as compared with those in all other directions.

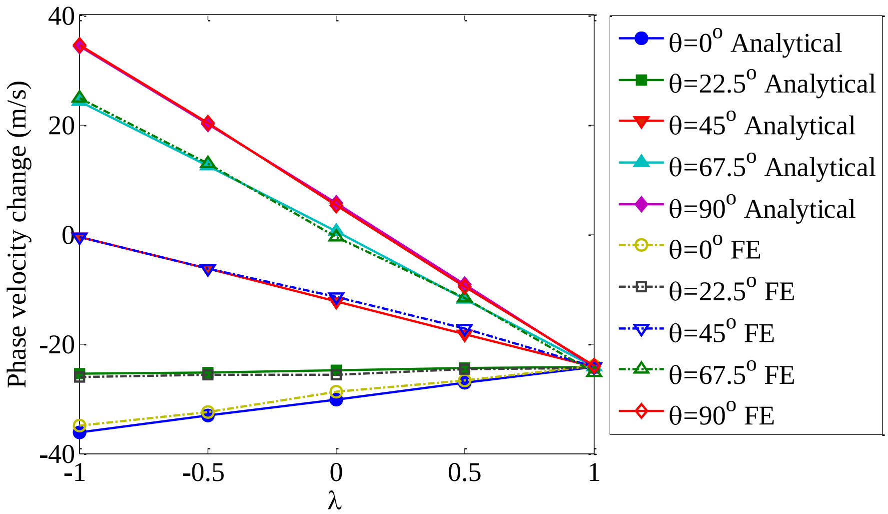

Figure 5: Phase velocity change for different values of stress ratio λ with *fd* = 800kHz-mm, σ_1 = 80MPa

Figures 6 and 7 show the effect of the stress magnitude on the phase velocity change of the S_0 Lamb wave. The values of σ_1 considered in Case 2 are 0MPa, 20MPa, 40MPa, 60MPa and 80MPa, and the bi-axial stress ratios λ are -1 and -0.5. This means that the σ_2 are 0MPa, -20MPa, -40MPa, -60MPa and -80MPa for λ = -1 as shown in Figure 6, and 0MPa, -10MPa, -20MPa, -30MPa and -40MPa for λ = -0.5 as shown in Figure 7. The same as Figure 5, there is very good agreement between the analytical solutions and FE simulation results in Figures 6 and 7. Figure 6 considers the stresses adding in x_1 and x_2 direction are of the same magnitude (λ = -1). Therefore, the values of the phase velocity change are the same in $\theta = 0°$ and 90°, and $\theta = 22.5°$ and 67.5°, respectively, but they are in opposite sign. There is no change in the phase velocity for $\theta = 45°$ regardless the changes in the applied stress. Different to Figure 6, Figure 7 considers λ = -0.5. The phase velocity change in $\theta = 45°$ is no longer equal to zero when bi-axial stress is applied on the plate. Also, the values of the phase velocity change for wave propagation at $\theta < 45°$ are larger than those at $\theta > 45°$. This is because the stress value in x_1 direction is always larger than x_2 in Case 2.

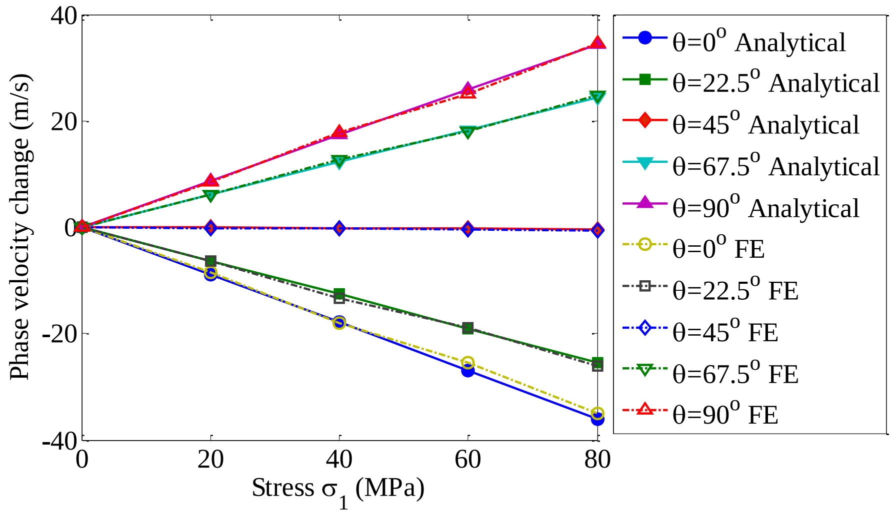

Figure 6: Phase velocity change for different stress levels with *fd* = 800kHz-mm, λ = -1

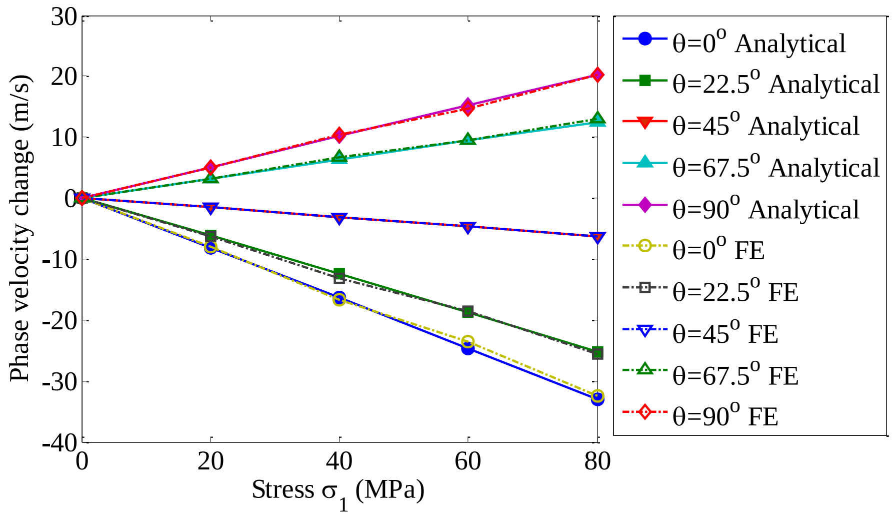

Figure 7: Phase velocity change for different stress levels with *fd* = 800kHz-mm, λ = -0.5

Figure 8 shows the phase velocity change in relation to the wave propagation angle. The wave propagation angles considered are $\theta = 0°, 22.5°, 45°, 67.5°$ and $90°$. Biaxial ratios λ = -1, -0.5, 0 , 0.5 and 1 while σ_1 = 80MPa are considered in Case 3. As shown in Figure 8, it is found that the phase velocity changes are always the same for different biaxial stress ratios when the propagation angle roughly is equal to 22.5°. When λ = 1, the phase velocity is the same for all wave propagation angle. Figure 9 shows the results of Case 4, in which are setting are the same, expect the excitation frequency is 200kHz. The phenomena of the phase velocity change in relation to the wave propagation angle and biaxial stress ratio are very similar. The results in Figures 8 and 9 show that there is good agreement between the analytical solutions and FE simulation results.

Overall, the FE simulation results from the model with VUMAT subroutine agrees very well with the analytical results in all considered cases. It can be observed that the tensile stress reduces the phase velocity while the compression increases the phase velocity of the S_0 Lamb wave. The phase velocity changes in different cases with different loads, propagation angles and stress ratios are quite different.

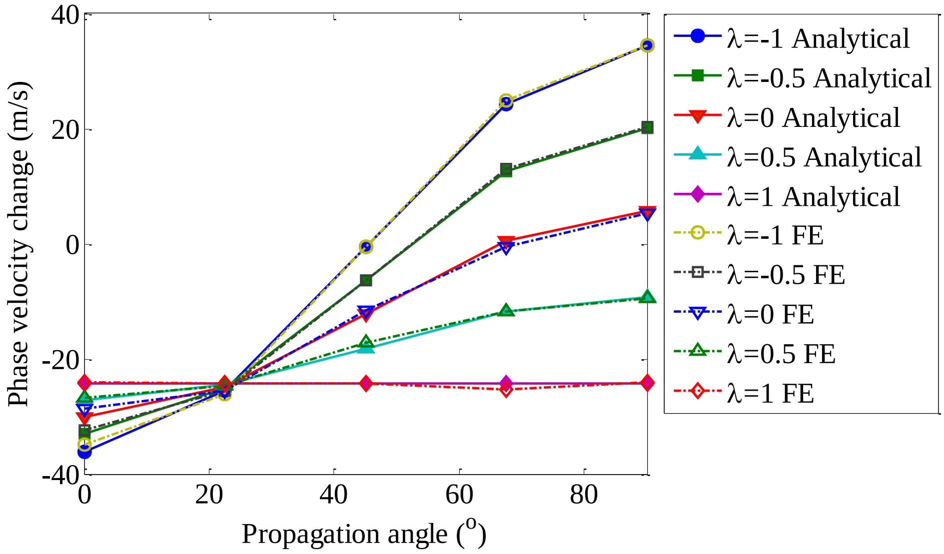

Figure 8: Phase velocity change for different wave propagation directions with *fd* = 800kHz-mm, σ_1 = 80MPa

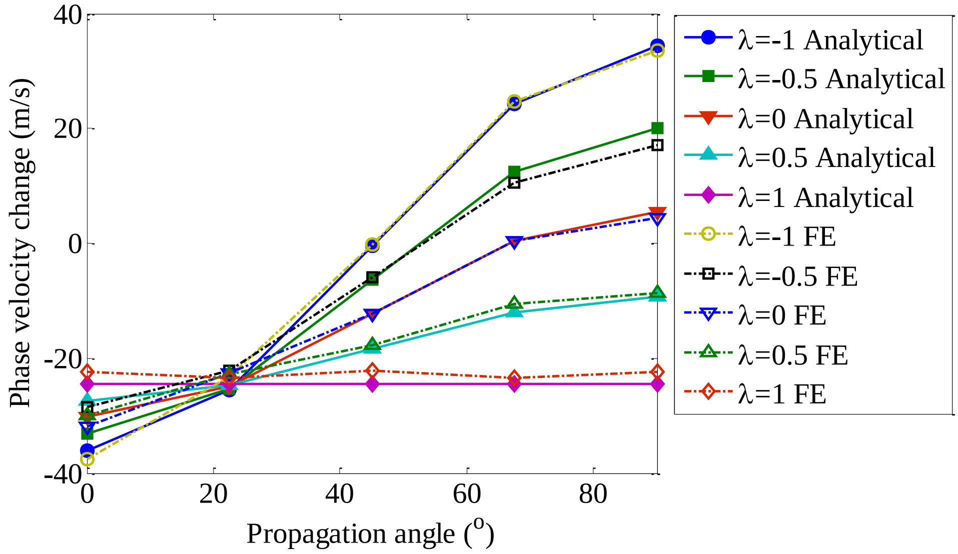

Figure 9: Phase velocity change for different wave propagation directions with *fd* = 640kHz-mm, σ_1 = 80MPa

5. Acoustoelastic effect of Lamb wave propagation under bending stress

5.1. Front shape of Lamb waves under applied bending stress

A 2D plane strain model is first developed in ABAQUS to investigate the variation of the front shape of S_0 Lamb wave propagation on a plate under a bending stress. The dimension of the plate is 1000mm long by 3.2mm thick. 4-node bilinear plane strain quadrilateral elements are used with reduced integration and hourglass control (CPE4R). The element size is 0.25mm in length and 0.32mm in depth to ensure there are at least 10 elements in the thickness direction and 20 elements per wavelength [51]. The excitation is a 250kHz 4-cycle narrow-band sinusoidal tone burst pulse modulated by a Hann window. The S_0 Lamb wave is excited at the middle of the plate. The bending stress is applied at both ends of the plate and varies linearly through the plate thickness. The material nonlinearity sub-routine is modified to accommodate the 2D plane strain condition. The measurement location is at 400mm away from the excitation location. At this location, both in-plane and out-of-plane displacements of the nodal points located along the plate thickness are calculated for the plate at stress free condition and the under a maximal bending stress of 80MPa. As shown in Figure 12, when the plate is free from bending stress, the in-plane displacement front shape of the S_0 Lamb wave is symmetric about the mid-plane of the plate, while the out-of-plane mode shape is antisymmetric. As compared, when the plate is under the bending stress, both in-plane and out-of-plane displacement front shapes are slightly distorted.

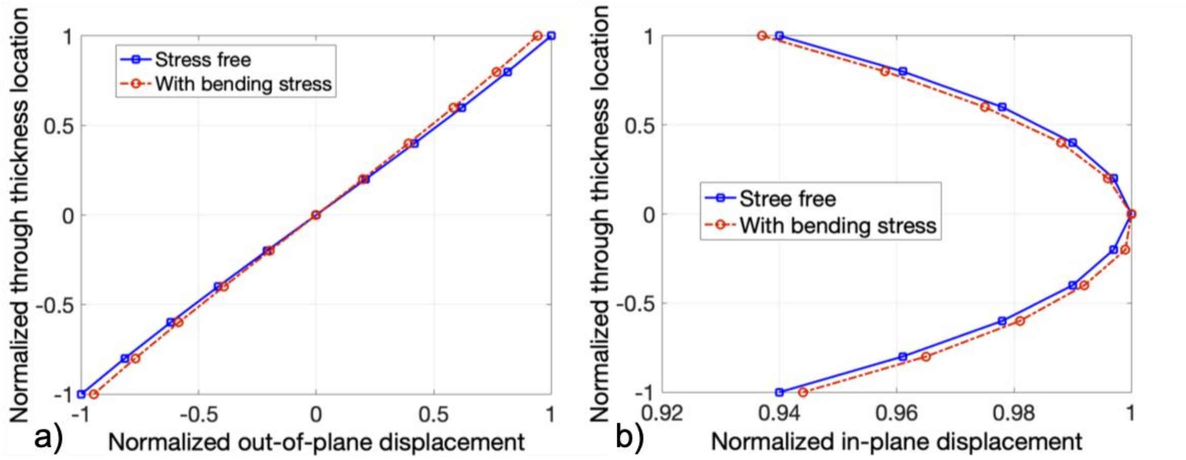

Figure 12: a): In-plane and b) out-of-plane displacement front shape with and without applied bending stress

5.2. Phase velocity change due to applied bending stress

In this section, the verified 3D FE model with material nonlinearity effect is applied to simulate the acoustoelastic effect on Lamb wave propagation in plate under bending stress. The 3D FE model has same properties (excitation frequency and location, boundary conditions, and FE mesh) as the one shown in Figure 2. Measurements are taken at the nodal points at the top, mid-plane and bottom of the plate. Bending stress is applied along the surface highlighted in Figure 10. The stress is applied with a pressure load with analytical field, which defines the linear variation of the pressure along thickness. The maximal magnitude of the stress is varied from 20MP to 80MPa.

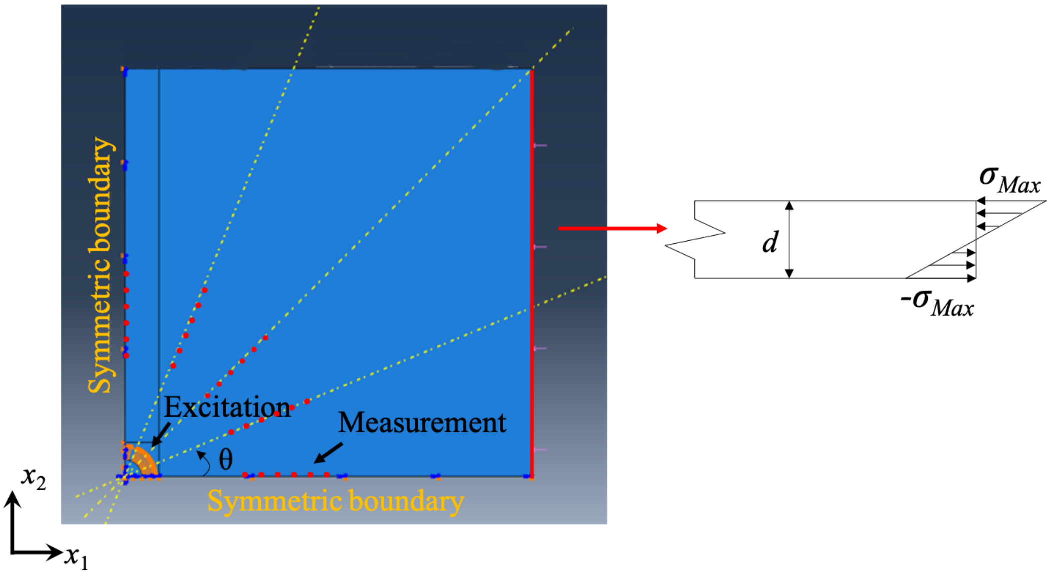

Figure 10. 3D FE model under bending stress

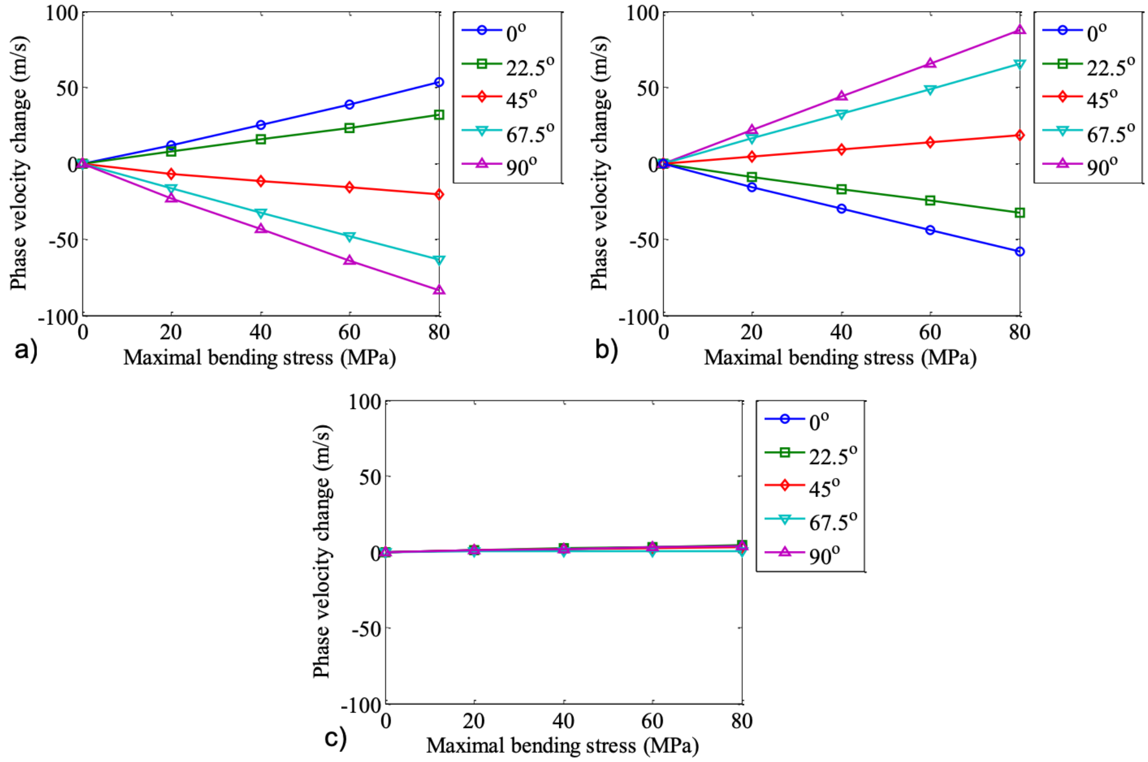

Figure 11. Phase velocity change with measurement calculated at the a) top, b) bottom, and c) mid-plane of the plate for different propagation directions and under different magnitudes of maximal bending stresses

Results of numerical simulations are shown in Figure 11. The dependence of the phase velocity change against the applied bending stress is linear in all propagation directions. Meanwhile, it should be noticed that, the phase velocity change obtained from the top and bottom of the plates in the same propagation direction under the same stress condition has very similar magnitudes but the opposite sign. In addition, as demonstrated in Figure 11c, the phase velocity changes are about zero in all directions for all stress conditions. The results indicate that the phase velocity change is caused by the applied bending stresses. The region above and below the mid-plane of the plate are under tension and compression, respectively. As a result, the phase velocity changes in Figures 11a and 11b have an opposite trend. At the location of the mid-plane, the stress is zero so the value of the phase velocity change is almost zero despite increasing the applied bending stress.

6. Conclusions

The study has presented outcomes of a numerical simulations of the acoustoelastic effect associated with S_0 Lamb wave propagation in a prestressed plate. The nonlinear material model has been formulated based on Murnaghan's energy function. A series of case studies have been conducted and the phase velocity changes from FEA have been compared with the analytical results. The 3D FE results have shown nearly perfect match with the analytical solutions for the all range of stress ratios, stress magnitudes and propagation angles. The results have indicated that the 3D FE model with VUMAT subroutine, is able to simulate the acoustoelastic effect due to the nonlinear characteristics of a material under pre-stressed condition. The study has also investigated a more complicated stress situation, when the plate is subjected to bending stress. The effects of the applied bending stress on the in-plane and out-of-plane displacement front shapes has been investigated. It has demonstrated that for short propagating distances the effect of bending stress is negligible and can be omitted from design considerations of defect detection system utilising the S_0 Lamb wave.

The main outcome of this study is that the 3D FE model with nonlinear material model can be used to accurately predict the acoustoelastic effect associated with the Lamb wave propagation in plates subjected to applied stress, including the cases when the plates are subjected to complicated stress state. In these cases, the analytically solution are not available and the only way to analyse these situations are direct numerical simulations. It is believed that the numerical simulations can contribute to the further developments of damage detection using Lamb waves as well as the on-line stress monitoring techniques. In addition, the model can also be used in developing SHM system. As it is proven that stress variation can affect the propagating waves, by considering the effect of loading conditions on linear guided wave propagation in practical field, and compensate this effect would help achieve a more accurate assessment of damages.

7. Acknowledgement

This work was supported by the Australian Research Council (ARC) under Grant Numbers DP160102233. The support is greatly appreciated.

8. References

[1] Pan J, Zhang Z, Wu J, Ramakrishnan KR, Singh HK. A novel method of vibration modes selection for improving accuracy of frequency-based damage detection. Composites Part B: Engineering, 2019, 159: 437-446.

[2] Zhou C, Zhang C, Su Z, Yue X, Xiang J, Li G. Health monitoring of rail structures using guided waves and three-dimensional diagnostic image. Structural Control and Health Monitoring, 2017, 24: e1966.

[3] Zhang Z, Zhang C, Shankar K, Morozov EV, Singh HK, Ray T. Sensitivity analysis of inverse algorithms for damage detection in composite. Composite Structures, 2017, 176: 844-859.

[4] Zhang Z, Shankar K, Morozov EV, Tahtali M. Vibration-based delamination detection in composite beams through frequency changes. Journal of Vibration and Control, 2016, 22:496-512.

[5] Yu L, Leckey CAC, Tian Z. Study on crack scattering in aluminium plates with Lamb wave frequency-wavenumber analysis. Smart Materials and Structures, 2013, 22: 065019.

[6] Dao PB, Staszewski WJ. Lamb wave based structural damage detection using cointegration and fractal signal processing. Mechanical Systems and Signal Processing, 2014, 49(1-2): 285-301.

[7] Soleimanpour R, Ng CT, Wang CH. Higher harmonic generation of guided waves at delaminations in laminated composite beam. Structural Health Monitoring, 2017, 16(4): 400-417.

[8] Alguri KS, Melville J, Harley JB. Baseline-free guided wave damage detection with surrogate data and dictionary learning. The Journal of the Acoustical Society of America, 2018, 143(6): 3807-3818.

[9] Zak A, Radzienski M, Krawczuk M, Ostachowicz W. Damage detection strategies based on propagation of guided elastic waves. Smart Materials and Structures, 2012, 21:035024.

[10] Mitra M, Gopalakrishnan S. Guided wave based structural health monitoring A Review. Smart Materials and Structures, 2016, 25:053001.

[11] Mohseni H, Ng CT. Higher harmonic generation of Rayleigh wave at debondings in FRP-retrofitted concfrete structures. Smart Materials and Structures, 2018, 27:105038.

[12] Mohseni H, Ng CT, Lam HF. Debonding detection in CFRP-retrofitted reinforced concrete structures using nonlinear Rayleigh wave. Mechanical System and Signal Processing, 2018, https://doi.org/10.1016/j.ymssp.2018.08.027

[13] Liu Y, Lin S, Li Y, Li C, Liang Y. Numerical investigation of Rayleigh waves in layered composite piezoelectric structures using the SIGA-PML approach. Composites Part B: Engineering, 2018, 158, 230-238.

[14] Ng CT. On accuracy of analytical modelling of Lamb wave scattering at delaminations in multilayered isotropic plates. International Journal of Structural Stability and Dynamics, 2015, 15(8): 1540010.

[15] Panda RS, Rajagopal P, Balasubramaniam K. Characterization of delamination-type damages in composite laminates using guided wave visualization and air-coupled ultrasound. Structural Health Monitoring, 2017, 16(2): 142-152.

[16] Memmolo V, Monaco E, Boffa ND, Maio L, Ricci F. Guided wave propagation and scattering for structural health monitoring of stiffened composite. Composite Structures, 2018, 184: 568-580.

[17] An YK, Sohn H. Integrated impedance and guided wave based damage detection. Mechanical Systems and Signal Processing, 2012, 28: 50-62.

[18] Yang Y, Ng CT, Kotousov A. Second harmonic generation of guided wave at crack-induced debonding in FRP-strengthened metallic plates. International Journal of Structural Stability and Dynamics, 2019, 19(1): 1940006.

[19] He J, Yuan FG. Lamb wave-based subwavelength damage imaging using the DORT-MUSIC technique in metallic plates. Structural Health Monitoring, 2016, 15(1): 65-80.

[20] He S, Ng CT. Guided wave-based identification of multiple cracks in beams using a Bayesian approach. Mechanical Systems and Signal Processing, 2017, 84: 324-345.

[21] Hu N, Shimomukai T, Yan C, Fukunaga H. Identification of delamination position in cross-ply laminated composite beams using S0 Lamb mode. Composites Science and Technology, 2008, 68(6): 1548-1554.

[22] He S, Ng CT. A probabilistic approach for quantitative identification of multiple delaminations in laminated beams using guided waves, Engineering Structures, 2016, 127: 602-614.

[23] Nasrollahi A, Deng W, Ma Z, Rizzo P. Multimodal structural health monitoring based on active and passive sensing. Structural Health Monitoring, 2018, 17(2): 395-409.

[24] Aryan P, Kotousov A, Ng CT, Cazzolato BS. A baseline-free and non-contact method for detection and imaging of structural damage using 3D laser vibrometry. Structural Control and Health Monitoring, 2017, 24: e1894.

[25] Liu C, Dobson J, Cawley P. Efficient generation of receiver operating characteristics for the evaluation of damage detection in practical structural health monitoring applications. Proceedings of The Royal Society A: Mathematical, Physical and Engineering Sciences, 2017, 473: 2199.

[26] Song Z, Qi X, Liu Z, Ma H. Experimental study of guided wave propagation and damage detection in large diameter pipe filled by different fluids. NDT & E International, 2018, 93: 78-85.

[27] Mohseni H, Ng CT. Rayleigh wave propagation and scattering characteristics at debondings in fibre-reinforced polymer-retrofitted concrete structures. Structural Health Monitoring, 2019, 18(1): 303-317.

[28] Rose JL. A baseline and vision of ultrasonic guided wave inspection potential. Journal of pressure vessel technology, 2002, 124(3): 273-282.

[29] Soleimanpour R, Ng CT. Locating delaminations in laminated composite beams using nonlinear guided waves. Engineering Structures, 2017, 131: 207-219.

[30] Attarian VA, Cegla FB, Cawley P. Long-term stability of guided wave structural health monitoring using distributed adhesively bonded piezoelectric transducers. Structural Health Monitoring, 2014, 13(3): 265-280.

[31] McKeon P, Yaacoubi S, Declercq NF, Ramadan S, Yaacoubi WK. Baseline subtraction technique in the frequency-wavenumber domain for high sensitivity damage detection, 2014, 54(2): 592-603.

[32] Aryan P, Kotousov A, Ng CT, Cazzolato B. A model-based method for damage detection with guided wave. Structural Control and Health Monitoring, 2017, 24: e1884.

[33] Sohn H. Effects of environmental and operational variability on structural health monitoring. The Royal Society Philosophical Transactions of The Royal Society A: Mathematical, Physical and Engineering Sciences, 2007, 365(1851): 539-560.

[34] Lanza di Scalea F, Salamone S. Temperature effects in ultrasonic Lamb wave structural health monitoring systems. The Journal of the Acoustical Society of America, 2008, 124(161): 161-174.

[35] Dao PB, Staszewski W. Cointegration approach for temperature effect compensation in Lamb-wave-based damage detection. Smart Materials and Structures, 2013, 22(9): 095002.

[36] Aryan, P, Kotouso A, Ng CT, Wildy S. Reconstruction of baseline time-trace under changing environmental and operational conditions. Smart Materials and Structures, 2016, 25: 035018.

[37] Liu Y, Kim JY, Jacobs LJ, Qu J, Li Z. Experimental investigation of symmetry properties of second harmonic Lamb waves, Journal of Applied Physics, 2012, 111: 053511

[38] He S, Ng CT. Modelling and analysis of nonlinear guided waves interaction at a breathing crack using time-domain spectral finite element method, Smart Materials and Structures, 2012, 26: 085002

[39] Yang Y, Ng CT, Kotousov A, Sohn H, Lim HJ. Second harmonic generation at fatigue cracks by low-frequency Lamb waves: Experimental and numerical studies, Mechanical Systems and Signal Processing, 2018, 99, 760-773

[40] Murnaghan FD. Finite deformations of an elastic solid. American Journal of Mathematics, 1937, 59(2): 235-260.

[41] Hughes DS, Kelly JL. Second-order elastic deformation of solids. Physical Review, 1953, 92(5): 1145.

[42] Egle DM, Bray DE. Measurement of acoustoelastic and third-order elastic constants for rail steel. The Journal of the Acoustical Society of America, 1976, 60(3): 741-744.

[43] Pau A, Lanza di Scalea F. Nonlinear guided wave propagation in prestressed plates. The Journal of the Acoustical Society of America, 2015, 137(3): 1529-1540.

[44] Mohabuth M, Kotousov A, Ng CT. Effect of uniaxial stress on the propagation of higher-order Lamb wave modes. International Journal of Non-Linear Mechanics, 2016, 86: 104-111.

[45] Gandhi N, Michaels JE, Lee SJ. Acoustoelastic Lamb wave propagation in biaxially stressed plates. The Journal of the Acoustical Society of America, 2012, 132(3): 1284-1293.

[46] Mohabuth M, Kotousov A, Ng CT, Rose LRF. Implication of changing loading conditions on structural health monitoring utilising guided wave. Smart Materials and Structures, 2018, 27:025003.

[47] Packo P, Uhl T, Staszewski WJ, Leamy MJ. Amplitude-dependent Lamb wave dispersion in nonlinear plates. The Journal of the Acoustical Society of America, 2016, 140(2): 1319-1331.

[48] Nayfeh, AH, Chimenti DE. Free wave propagation in plates of general anisotropic media. Journal of Applied Mechanics, 1989, 56, 881-886.

[49] Asay JR, Guenther AH. Ultrasonic studies of 1060 and 6061-T6 aluminum, Journal of Applied Physics, 1967, 38, 4086-4088.

[50] Yang Y, Ng CT, Kotousov A. Influence of crack opening and incident wave angle on second harmonic generation of Lamb waves. Smart Materials and Structures, 2018, 27: 055013.

[51] Moser F, Jacobs LJ, Qu J. Modeling elastic wave propagation in waveguides with the finite element method. NDT&E International, 1999, 32(4): 225-234.